Supplementary Materials for

Recent tropical Andean glacier retreat is unprecedented in the Holocene

Andrew L. Gorin *et al*.

Corresponding author: Andrew L. Gorin, andrew_gorin@berkeley.edu

Science **385**, 517 (2024)
DOI: 10.1126/science.adg7546

The PDF file includes:

Materials and Methods
Supplementary Text
Figs. S1 to S12
Tables S1 to S6
References

Materials and Methods

1. Field Methods

Bedrock samples were collected with a hammer and chisel, and topographic shielding was estimated with an inclinometer. Samples from local high points were favored where possible because this minimizes the chance that they were buried under till for extended periods of time. See figs. S1-S4 for photos of sample sites and table S1 for sample information.

2. Sample Processing and Measurement

Quartz was isolated from bedrock samples at Boston College. Whole-rock samples were crushed, magnetic minerals were removed with a Frantz magnetic separator, and feldspars and micas were removed by suspending the remaining fraction in a frothed flotation solution consisting of carbonated water, acetic acid, and laurel amine. A series of dilute HNO_3-HF etches dissolved remaining minerals and removed meteoric ^{10}Be from the quartz (*48*). 5-40 g of quartz was used for ^{10}Be analysis and 2-5 g of quartz for ^{14}C analysis.

Beryllium was extracted from quartz following routine chemical procedures (*48, 49*). Charquini Norte Glacier samples were processed at Tulane University, and Queshque Glacier, Pan de Azucar Glacier, and Zongo Glacier samples were processed at the University of Wisconsin-Madison. One or two process blanks were run with each batch. $^{10}Be/^{9}Be$ ratios were measured at PRIME Lab and calibrated against the Revised ICN Standard (07KNSTD) following the protocol outlined by PRIME Lab (table S2).

We extracted ^{14}C using the automated process outlined in Goehring et al. (*50*) at Tulane University. Carbon isotope ratios were measure by AMS at the National Ocean Sciences Accelerator Mass Spectrometer at Woods Hole Oceanographic Institution relative to the Oxalic Acid II primary standard (NIST SRM4990C) (table S3).

3. Blank Correction

Measured ^{10}Be concentrations were corrected with either the average and standard deviation of the process blanks measured during each batch (for batches with multiple blanks), or the measured blank value and uncertainty (for batches with only one blank). ^{10}Be blanks represent no more than 40% of the total nuclide abundance of the sample (fig. S5, table S4).

^{14}C samples were corrected with a lognormal distribution fit to all blank measurements made in the Tulane lab from 2019 to 2022 (n=50; fig. S5) using a Monte Carlo routine (*51*). Blank values were randomly drawn from this distribution 100,000 times and subtracted from measured sample ^{14}C abundances drawn from within their uncertainty range. We report the 50th percentile blank-corrected concentration and the 68% confidence interval. This uncertainty distribution is asymmetric with a lower uncertainty bound of zero on most samples, reflecting the long tail of high blank values (table S3).

4. Nuclide Concentrations as Years

Nuclide concentrations were converted to years of equivalent surface exposure using production rates from the University of Washington online cosmogenic calculator

v3 with the LSDn scaling scheme and global production rate calibration dataset (table S5) (*52*, *53*). Nuclide concentrations were divided by the effective production rate, accounting for sample thickness and topographic shielding.

5. Historical Ice Margins

Historical ice margins shown in Fig. 2 are from Rabatel et al. (*54*) for Charquini Norte Glacier, (*21*) for Queshque Glacier, and Soruco et al. (*55*) for Zongo Glacier. The 2012 margin for Queshque Glacier and 2009 margin for Pan de Azucar Glacier were drawn using Google Earth images. These historical margins were used to estimate when samples were exposed by recent retreat and correct measured nuclide concentrations for this recent exposure (table S5).

6. Cosmogenic Nuclide Forward Model

We developed a numerical model to simulate nuclide production, decay, erosion, and ice of varying thicknesses associated with various possible glacier histories (*19*). The model simulates a bedrock depth profile of ^{10}Be and ^{14}C concentrations through time, driving production when exposed and erosion when ice covered; decay occurs continuously. During periods of burial, we choose an ice thickness, and calculate the production rate at depth below this amount of ice assuming an ice density of 0.917 g/cm^3 (*56*). Production rate profiles are derived from the University of Washington online cosmogenic calculator v3 (*53*) using the LSDn scaling scheme (*52*) with the global production rate calibration dataset (fig. S6). The evolution of nuclide concentrations in a bedrock column are then calculated in 100-year time steps via equation 1.

$$N(z,t) = P_{NT}(z) + N(z,t-1) * e^{-\lambda_N t} \quad (1)$$

Where N is the concentration of the nuclide in the bedrock as a function of depth (z) and time (t), P_{NT} is the total production of the nuclide via spallation and muon production as a function of depth, and λN is the decay constant of the nuclide. During times of exposure, the model uses the production portion of equation 1 (left of the addition sign). During times of burial, the model only uses the decay portion of equation 1 (right of the addition sign). Erosion is incorporated by redefining the "surface" as some depth below the top of the bedrock. The model assumes that erosion only takes place during times of burial.

We model two sets of scenarios to explore possible interpretations of the near-zero nuclide concentrations measured in tropical proglacial bedrock. The first set simulates nuclide production through ice cover of constant thickness over 50 kyr (i.e., surface exposure does not occur) (fig. S7). The simulations assume zero erosion. ^{14}C accumulates rapidly in the first 10 kyr and approaches secular equilibrium within ~25 kyr. ^{10}Be accumulates continuously and near-linearly due to negligible decay. ^{14}C and ^{10}Be concentrations similar to those we measured (~10 to 200 years surface-exposure equivalent for ^{14}C and ~10 to 60 years for ^{10}Be) accumulate under ice thicknesses of 10-60 m, though more time is required for ^{10}Be than ^{14}C.

The second set of scenarios simulate a two-stage Holocene history (10 – 0 ka), with an interval of exposure followed by an interval of burial to the present (fig. S8). We base this generalized glacier evolution on data compilations suggesting tropical glaciers were generally smaller earlier in the Holocene and larger later in the Holocene (*7*, *33*).

The durations of these two intervals are systematically adjusted by 1 kyr to produce a range of exposure histories (i.e., 9 kyr of exposure followed by 1 kyr of burial, 8 kyr of exposure followed by 2 kyr of burial, etc.). Nuclide production only occurs during the exposure interval. Each history is rerun for erosion rates ranging from 0-1 mm/yr. Erosion rates of at least 0.25 to 1 mm/yr are needed to reduce nuclide concentrations to the low levels we measured in proglacial bedrock. As we discuss in the next section, these are unrealistically high erosion rates for the glaciers we studied.

In addition to these hypothetical glacier simulations, we also use the model to constrain plausible Holocene exposure histories compatible with the two down-valley samples we measured at Charquini Norte with relatively high ^{14}C and ^{10}Be concentrations and low $^{14}C/^{10}Be$ ratios. We tested 100,000 quasi-randomly generated exposure histories, each run for a wide range of subglacial erosion rates (see (*19*) for details on generating histories). Only 1,567 histories produced nuclide concentrations consistent with the measured values (i.e., within 3σ) and all show exposure in the early Holocene (~10-7 ka) followed by continuous burial (fig. S9). Conceptually, several kyr of exposure are needed to produce the relatively high nuclide concentrations, while continuous burial for the rest of the Holocene is then needed to allow ^{14}C concentrations to decrease substantially relative to ^{10}Be due to decay. Subglacial erosion rates associated with these successful simulations have a 95% confidence interval of 0 to 0.15 mm/yr.

7. Glacier Erosion Rates

We estimated erosion rates, $\dot{E}$, for the four glaciers in our study, as well as eight glaciers from prior studies (two in the tropics, six in the mid latitudes) where proglacial bedrock ^{14}C-^{10}Be measurements have been made (table S6). These calculations use the following scheme: *1.* Modern (~2000 CE) glacier thickness (*57*) and slope (*58*) are used to estimate a gravitational driving stress $\overline{\tau_d}$ which is set equal to the average basal shear stress, $\overline{\tau_b}$; *2.* Apply a shape correction factor to account for drag on valley walls in order to isolate the portion of driving stress that goes into basal slip using equation 2 and so erodes the bed material; *3.* Apply two slip laws equation 3a for Weertman (*59*) plastic deformation and 3b from Helanow et al., (*60*) for sliding with cavitation to translate driving stress to sliding speed using (*59, 60*); *4.* Multiply the resulting sliding speed by the shear stress ($\overline{\tau_b} U_b$) to estimate basal power; *5.* Use the power to estimate the erosion rate, $\dot{E}$, with a recent model (*35*) with equation 4.

$$\overline{\tau_b} = -S_f \rho g H \cdot \tan(\alpha) \qquad (2)$$

$$U_b = lb\left(\frac{\overline{\tau_b}}{Br^2}\right)^n \qquad (3a)$$

$$U_b = \frac{A_s C^n N^n \left(\frac{\overline{\tau_b}}{NC}\right)^n}{1-\left(\frac{\overline{\tau_b}}{NC}\right)^n} \qquad (3b)$$

$$\dot{E} = \overline{\tau_b} U_b \mathbb{C} K \qquad (4)$$

where S_f is the shape factor here set to 0.5, ρ is the density of ice = 920 kg m^{-3}, g is the gravitational constant = 9.81 m s^{-2}, H is the ice thickness in meters, α is the slope in

degrees, l is the controlling bump height here set to 0.1 m, b is the zone over which the deviatoric stress affects the strain rate, here set to 3 following Zoet and Iverson (*61*), B is the ice viscosity set to 6.3×10^7 Pa $s^{1/3}$, n is the exponent on the ice flow law here set to 3, r is roughness of the bed here set to 0.3 (*62*), A_s depends on the ice rheology and morphology of the bed and is set to 20756 (*60*), C is a fitting parameter set to 0.3 (*60*), N is the basal effective pressure equal to $\rho g H$ multiplied by the floatation factor which is set to 0.9 (*60*), $\mathbb{C}$ is the debris concentration in the basal ice set to 0.1 and K is the erodibility of the rock set to 1.6×10^{-10} Pa^{-1} (*35*).

We confirmed the validity of this scheme in two ways. First, we compared the predicted abrasion rates for seven glaciers from prior work as well as for Charquini Norte Glacier to direct constraints from 14C-10Be measurements on recently exposed bedrock at these glaciers (using the mean and standard deviation). Note that no constraints were provided from the measurements made at Conness Glacier, as the nuclide concentrations were too low. The estimates agree well, with most overlapping at one standard deviation and all overlapping at two standard deviations (fig. S10). Second, we compared predicted values to results from more complex modeling at one of our glaciers (Zongo). There, surface velocities based on two decades of monthly stake measurements combined with two ground penetrating radar campaigns made it possible to calibrate a 3-D full-Stokes ELMER ice model and determine basal shear stresses and sliding velocities (*36*). These yield an average basal power for the glacier of 0.08 W, in general agreement with our estimates (0.09 and 0.10 W using the Helanow and Weertman slip laws, respectively).

The abrasion rates we estimated, 0.001 to 0.15 mm/yr, are on the lower end of commonly cited glacial erosion rates in the literature, which can exceed 10 or even 100 mm/yr (*34*, *63*). We attribute this apparent discrepancy to a few factors. First, our estimates only account for abrasion, whereas most values in the literature reflect total glacial erosion (abrasion + quarrying). This point can be illustrated with one of the glaciers in our compilation (Rhone). Rhone Glacier erosion rates constrained by cosmogenic nuclides in river sediments (2.1 ± 1.7 mm/yr) (*64*, *65*) are an order of magnitude higher than abrasion rates based on both our basal power modeling (0.049 and 0.11 mm/yr) and ^{14}C-^{10}Be measurements in proglacial bedrock (0.02 to 0.33 mm/yr) (*17*). The lower abrasion-only values are more appropriate for our samples because we targeted abraded bedrock and avoided areas of obvious glacial plucking. Second, constraints on glacial erosion rates exhibit a time scale bias, decreasing by roughly 100-fold from decadal to orogenic time scales (*63*, *65*). Many of the highest erosion rates in the literature apply to decadal time scales (e.g., from gauging of meltwater streams), and may be especially high because they reflect the recent period of glacier retreat (*63*). These high rates are therefore not relevant to the Holocene time scales recorded by our samples. Third, these high erosion rates also generally come from large, fast-flowing tidewater glaciers in e.g., Alaska and Patagonia, and for this reason are also probably not applicable to the smaller, slower Andean glaciers in our study.

Supplementary Text

8. Prior Constraints on Holocene Glacier Histories

Pan de Azucar Glacier

This 1.5 km^2 glacier is located in the Sierra Nevada del Cocuy in northeastern Colombia (6.4°N, 72.3°W). Modeling suggests that glaciers in this region (i.e., wet inner tropics) are particularly sensitive to changes in temperature as opposed to changes in precipitation (*20*). During the last 50 years, Colombian glaciers lost 50% of their area, and analyses show that high-altitude temperature has increased by greater than 1°C over the same period (*23*).

Jomelli et al. (*25*) developed a ^{10}Be chronology at Ritacuba Negro Glacier, 10 km north of Pan de Azucar Glacier, helping to constrain the Holocene glacial history in the region. A series of late glacial moraines indicate the glacier was 3-3.5 km longer than today from 14-11 ka. Two moraines slightly further upvalley record late Holocene advances at 1.2 ± 0.1 ka and 0.3 ± 0.02 ka, at which point the glacier began retreating from its Little Ice Age maximum, 2.5 km from the modern ice margin. The absence of deposits between these two moraine sets suggests the glacier was smaller than its Little Ice Age extent from ~11-1 ka.

Pollen and clastic sediment records from four lakes in the Cordillera de Merida (~275 km northeast of Pan de Azucar Glacier) provide more continuous histories of vegetation and glacier changes in the region from 15 ka to present. The pollen record indicates the highest elevations were unvegetated until about 11 ka, consistent with extensive ice before the Holocene (*66*). Between 12.6 and 9.5 ka, the influx of glacial sediments to many lakes declined, and ceased completely in locations that are presently unglaciated. From 4 ka until the LIA, the pollen record indicates a cooling trend while glaciogenic sediment fluxes to lakes with headwalls above 4,600 m increased, consistent with growing glacier sizes during this period (*66*, *67*). This is in contrast with lakes below lower elevation headwalls, whose clastic sediment fluxes remained constant (*67*). These records are consistent with the cosmogenic chronology from Pan de Azucar Glacier, suggesting that, following Late Glacial retreat, ice extent was relatively small during the early and middle Holocene but expanded during the late Holocene.

Queshque Glacier

This is a 1.7 km^2, southwestern-facing glacier located in the Cordillera Blanca of western Peru (9.8°S, 77.3°W). A combination of aerial imagery and digital elevation data suggests that the glacier lost 35% of its area and averaged 22 m of surface lowering between 1962 and 1999 (*9*). An accompanying heuristic sensitivity analysis shows that the 0.26°C/decade warming recorded at 29 stations in the Cordillera Blanca over the same interval is sufficient to account for this loss (*21*).

^{10}Be dating of moraines and clastic sediment records from two lakes immediately downvalley from Queshque Glacier offer insight into its past extent fluctuations (*27*, *69*). Moraine ages indicate the Late Glacial ice extent was largest at 13.8 ± 0.4 ka, and that the glacier generally retreated during the early Holocene, from 7 km beyond the modern ice margin at 10.8 ± 0.1 ka to 3.5 km at 9.4 ± 0.3 ka. An absence of moraines and decreasing glaciogenic sediment fluxes suggest the glacier was less extensive through the middle Holocene. Finally, scattered ^{10}Be ages of 3.5 ± 0.1 ka to 0.25 ± 0.01 ka on moraine boulders 2 km from the modern ice front, along with rising clastic sediment fluxes to the lakes, suggest the glacier readvanced in the late Holocene, with the most extensive advance within the past 0.5 kyr.

Charquini Norte and Zongo Glaciers

Charquini Norte (16.29°S, 68.10°W) and Zongo Glaciers (16.27°S, 68.13°W) are 0.1 and 1.9 km^2 respectively and located across a valley from one another in northwestern Bolivia. Zongo Glacier has lost approximately 0.15 km^2 of its surface areas since 1940 (*22*) and Charquini Norte has lost approximately 0.4 km^2 of its surface area during the same period (*22*, *54*). Over the last two decades of the 20th century, the rate of retreat at Charquini Norte Glacier increased by a factor of four (*54*). While weather station records indicate that precipitation in western Bolivia and eastern Peru has decreased slightly, temperatures have increased by more than 1°C over the last century (*22*, *70*). This suggests a larger role for temperature than precipitation in the overall mass balance changes.

^{10}Be ages on moraines at Charquini Norte Glacier and the adjacent Charquini Sur Glacier help constrain the Holocene glacial history (*26*). At Charquini Sur, there is a Little Ice Age moraine dated to 0.42 ± 0.02 ka just inboard of an early Holocene moraine with an age of 10.0 ± 0.21 ka, ~1.25 km from the modern ice margin. Similarly, Charquini Norte has two stages of moraines ~1.5 km down-valley from the current ice margin, the outer dated to 10.10 ± 0.26 ka and the inner dated to 1.20 ± 0.12 ka, just distal to a presumed Little Ice Age moraine from the past few centuries. Additional support for this Holocene glacial history comes from Jomelli et al. (*24*), who ^{10}Be dated an analogous set of early and latest Holocene moraines at Telata Glacier, 5 km north of Charquini.

9. Glacier Thicknesses

Two studies recently estimated ice thicknesses for the world's glaciers. Farinotti et al. (*57*) inferred ice thickness using observed glacier surface topography together with principles of ice flow. Millan et al. (*71*) calculated ice velocities and implied thicknesses based on 2017-2018 satellite image pairs. Farinotti et al.'s (*57*) data product includes all four of the glaciers we studied, while Millan et al. (*71*) only includes three (not Pan de Azucar Glacier) (figs. S11 and S12). Charquini Norte is extremely thin, at most a few tens of meters in places. Ice thicknesses are several tens of meters across most of Queshque and Zongo Glaciers and up to ~100 m along their centerlines, in good agreement with GPR-measured thicknesses at Queshque from 2009 (*72*). Queshque ice thicknesses modeled for its 1962 margin show our sample sites under ~100 m of ice (*72*), which may help explain why they have the lowest ^{10}Be concentrations in our dataset after correcting for recent exposure (Fig. 3B). Zongo ice thickness changes inferred from photogrammetry indicate that the lower tongue of the glacier was ~50-80 m thick across most of its width in 1956 and rapidly thinned toward its edges over our sample sites (*55*). Pan de Azucar Glacier is a veneer of ice draped over a narrow, gently sloping plateau bounded by cliffs, rather than a topographically confined valley glacier, which helps limit its thickness. The Farinotti et al. (*57*) data product suggests that the lower half of Pan de Azucar Glacier is <50 m thick and it thins radially toward the edges of the plateau where our samples are located. Overall, we conclude that the glacier thicknesses are broadly consistent with our interpretation that the low nuclide concentrations in recently exposed proglacial bedrock accumulated via muogenic production under tens of meters of continuous Holocene ice cover.

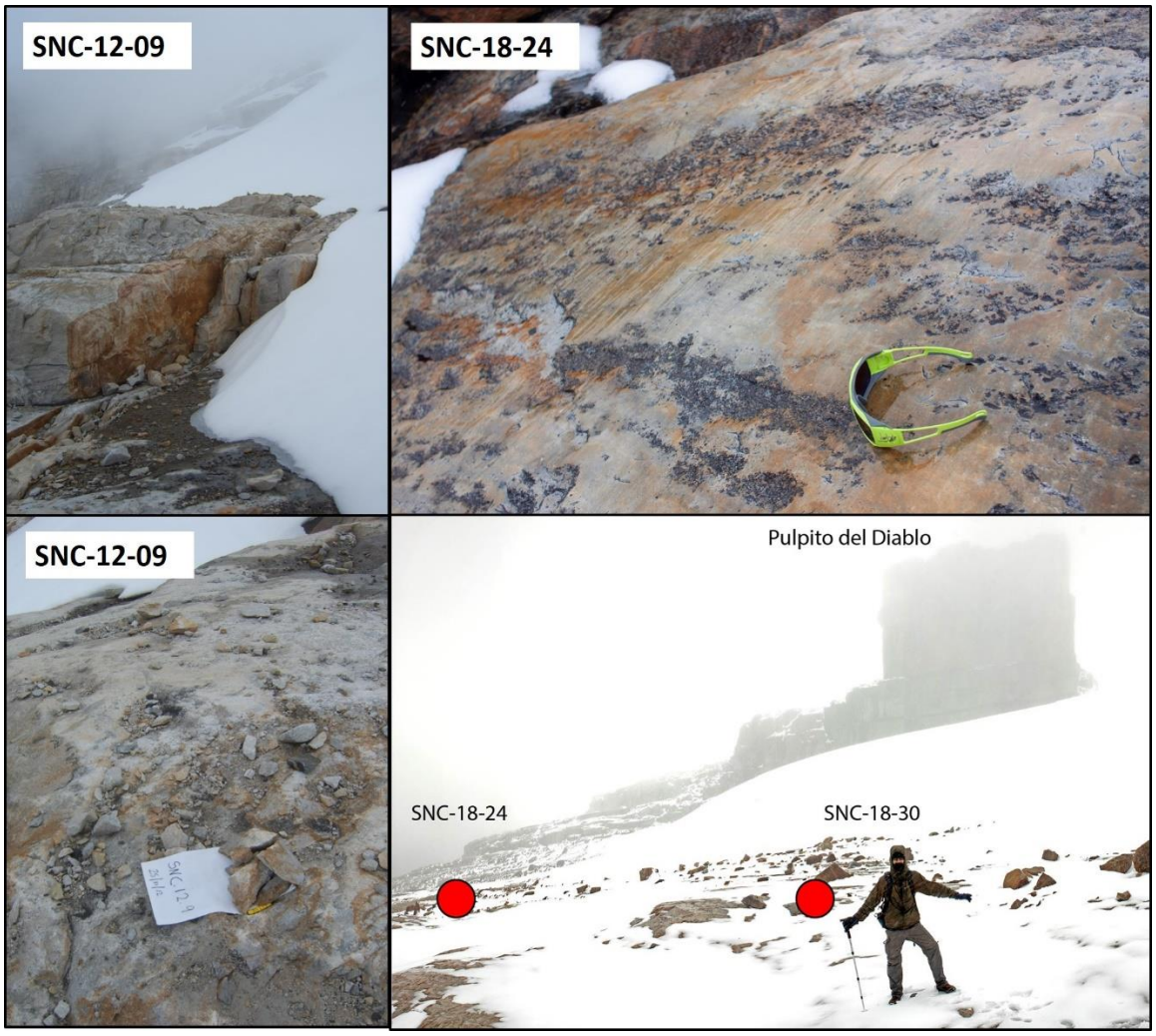

Fig. S1.
Photos of bedrock sample sites at Pan de Azucar Glacier.

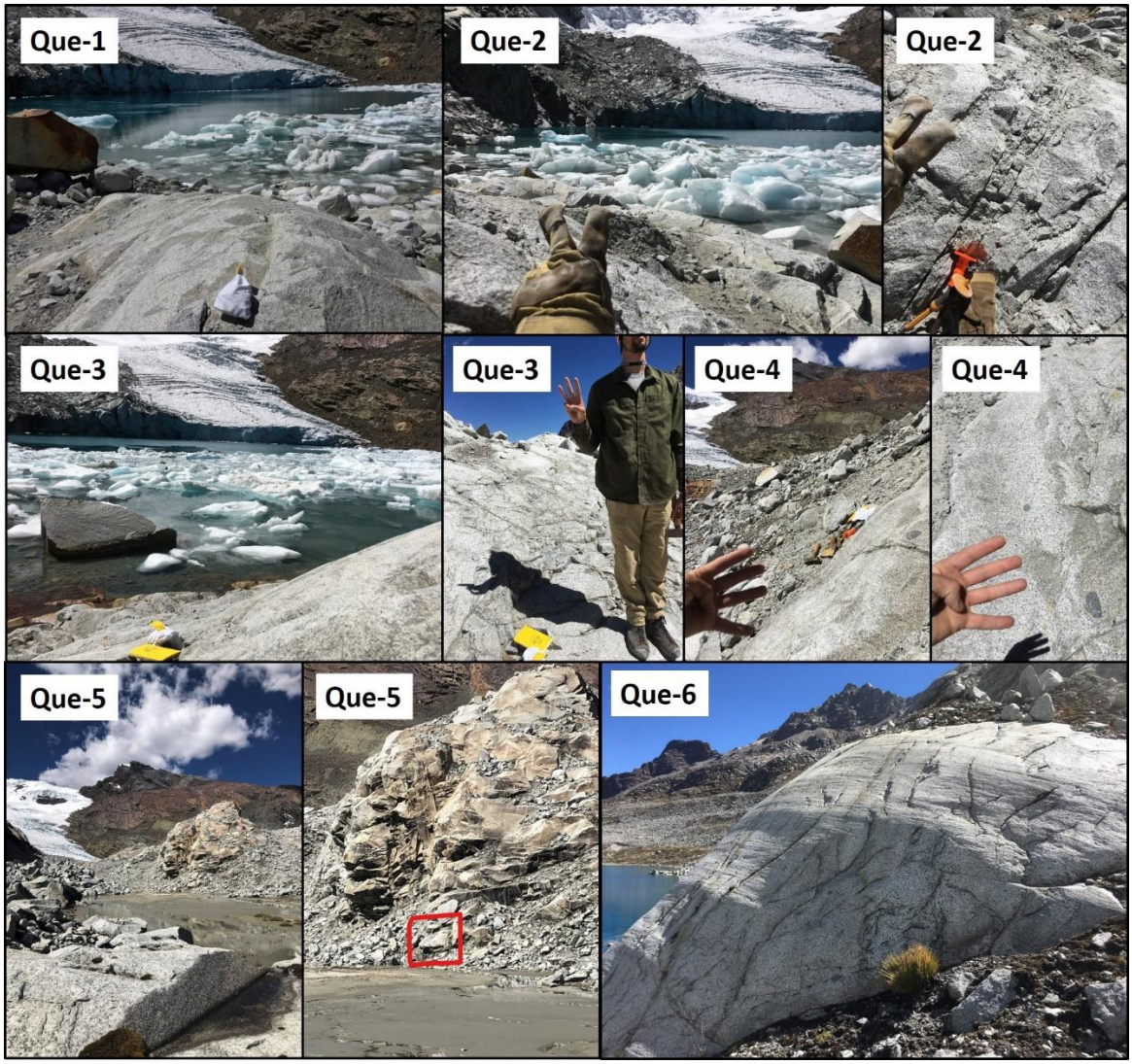

Fig. S2.
Photos of bedrock sample sites at Queshque Glacier.

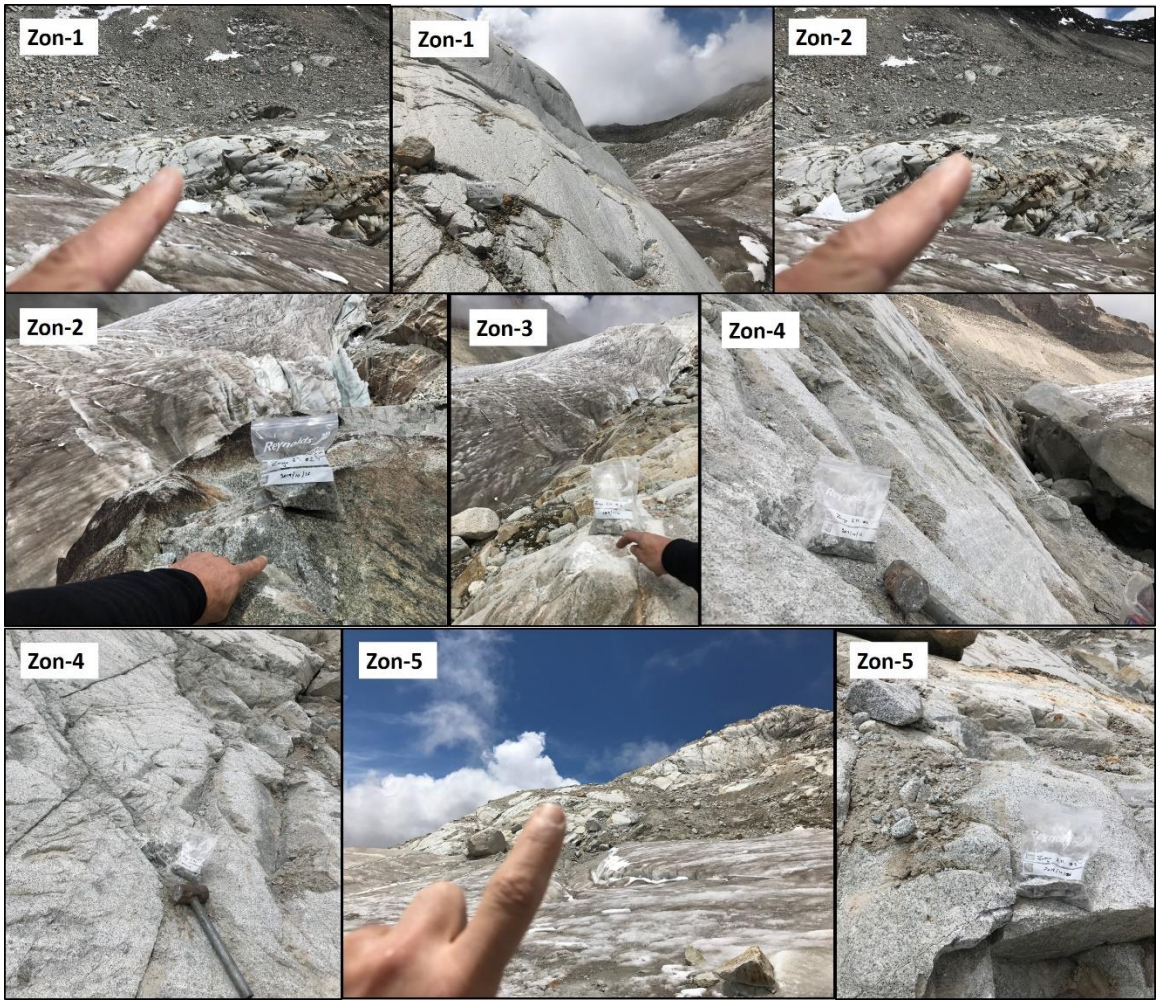

Fig. S3.
Photos of bedrock sample sites at Zongo Glacier.

Fig. S4.
Photos of bedrock sample sites at Charquini Norte Glacier.

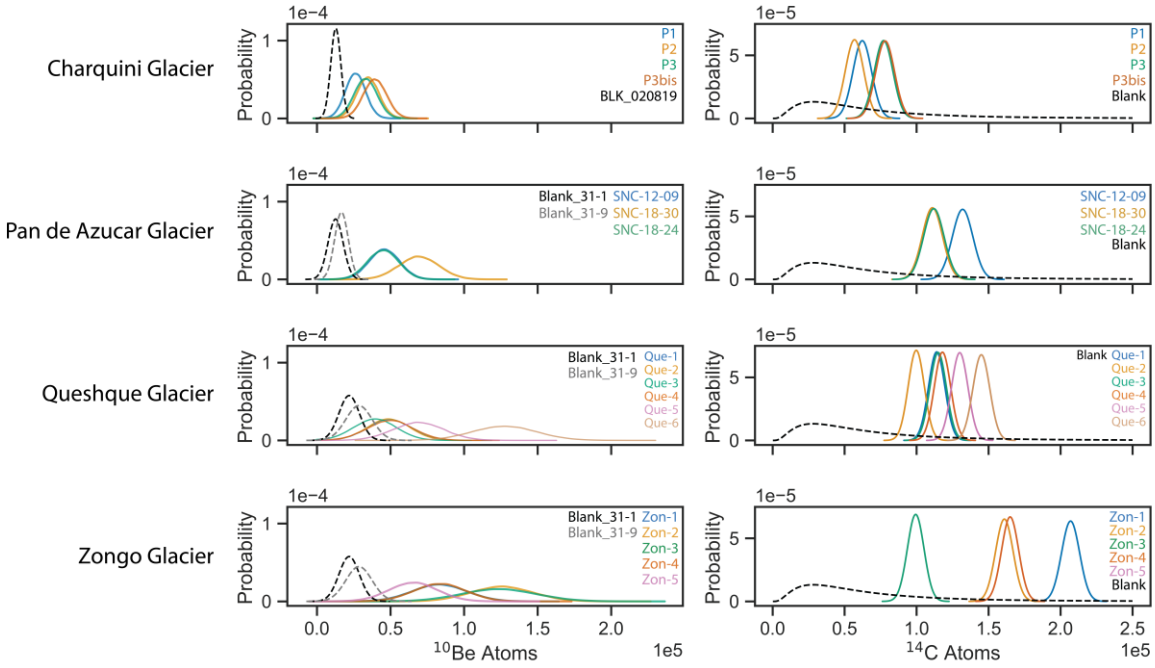

Fig. S5.

Measured ^{10}Be and ^{14}C nuclide abundances for each sample (solid lines) compared to laboratory process blanks (dashed lines). For ^{14}C, 'blank' indicates effective blank from a long-term, Monte Carlo-based background correction scheme (*51*). Each row represents a given glacier. The Zongo Glacier ^{14}C outlier (Zon-5) and the two down-valley Charquini samples (P12 and P13) are not shown as their concentrations do not approach blank level.

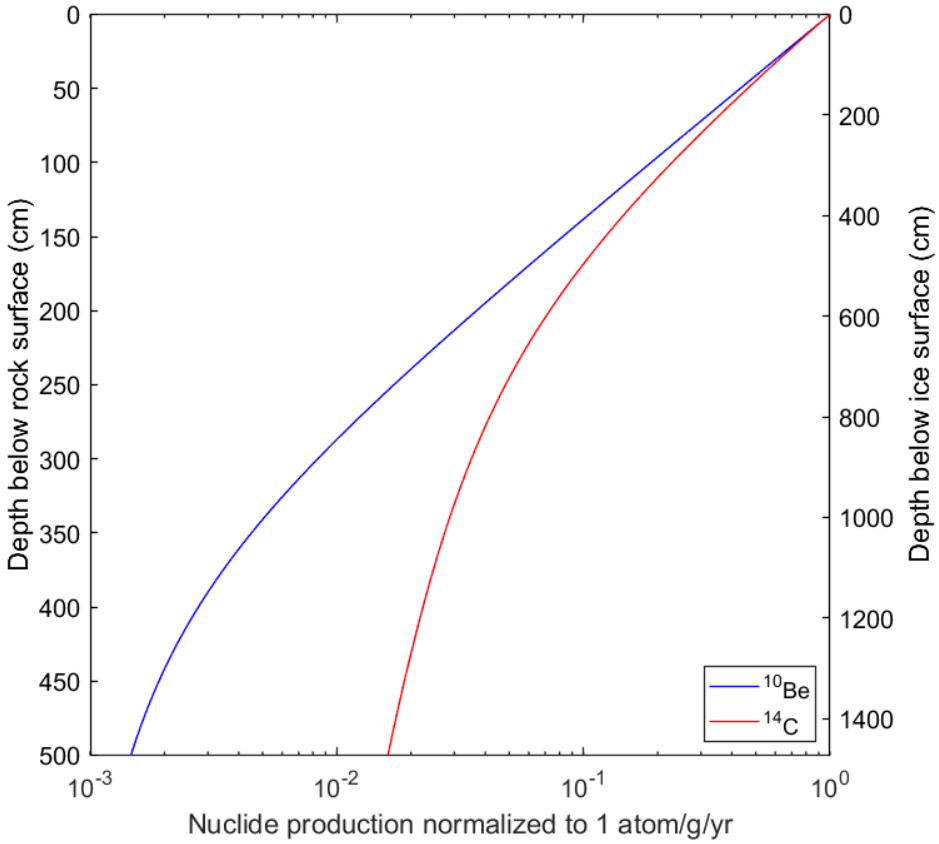

Fig. S6.
^{14}C and ^{10}Be production rate attenuation with depth in bedrock (density = 2.7 g/cm^3) in a low-latitude, high-elevation area. Profiles are derived from the University of Washington online cosmogenic calculator v3 (*53*) using the LSDn scaling scheme (*52*) with the global production rate calibration dataset.

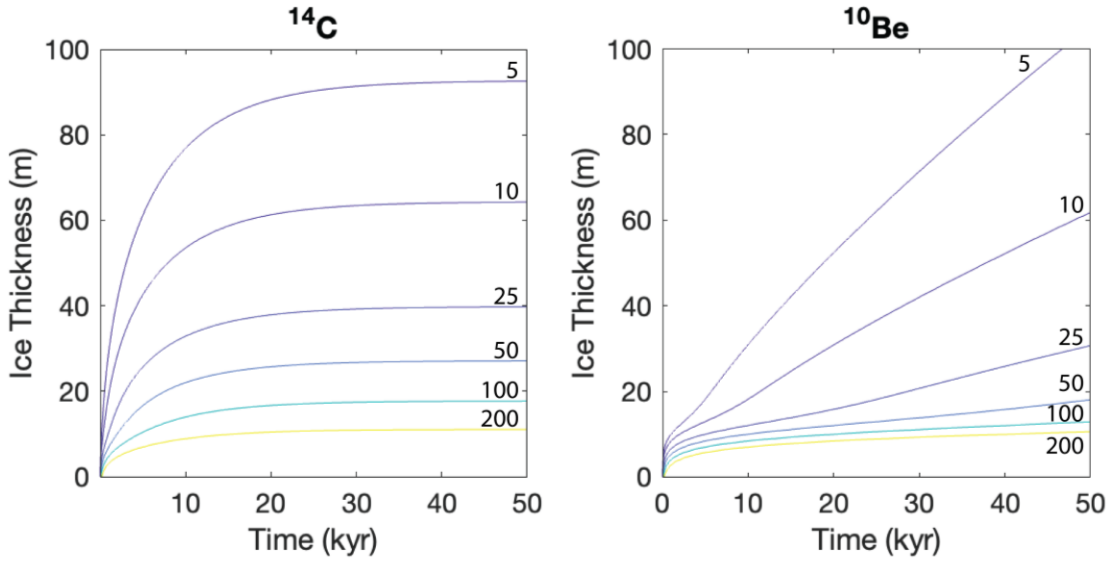

Fig. S7.
(**A**) Simulated evolution of bedrock surface ^{14}C concentrations under ice cover as a function of ice thickness. Erosion is assumed to be zero. (**B**) Same as panel A but for ^{10}Be. Lines are labeled with nuclide concentrations normalized by the surface production rate which are therefore equivalent to years of surface exposure.

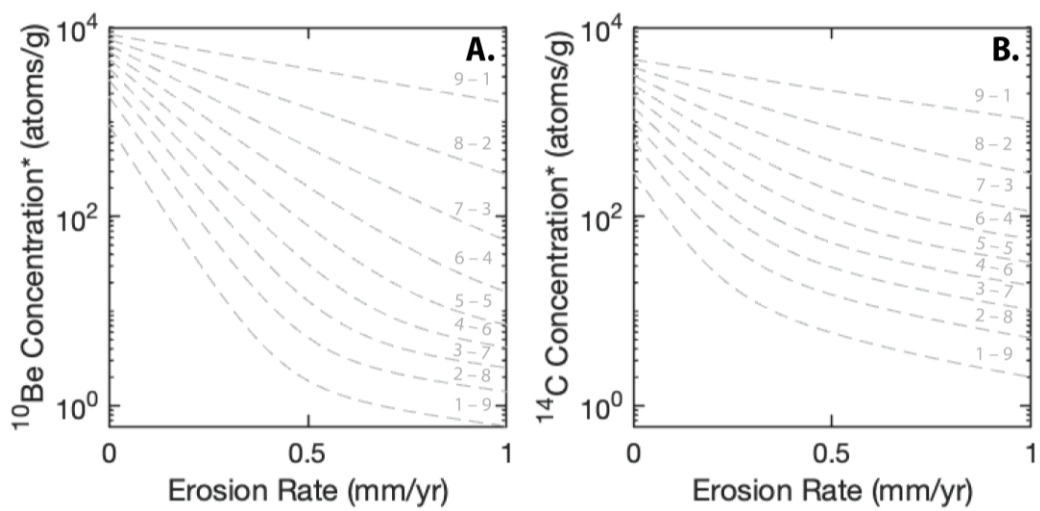

Fig. S8.
(**A**) Simulated bedrock surface ^{10}Be concentrations resulting from various 10 kyr-long exposure histories as a function of subglacial erosion rate. Each exposure history features an interval of exposure followed by an interval of burial (e.g., "9-1" means 9 kyr of exposure followed by 1 kyr of burial). Calculations do not include nuclide production through ice during burial or erosion during exposure. (**B**) Same as panel A but for ^{14}C. Nuclide concentrations are normalized by the surface production rate and are therefore equivalent to years of surface exposure for ^{10}Be.

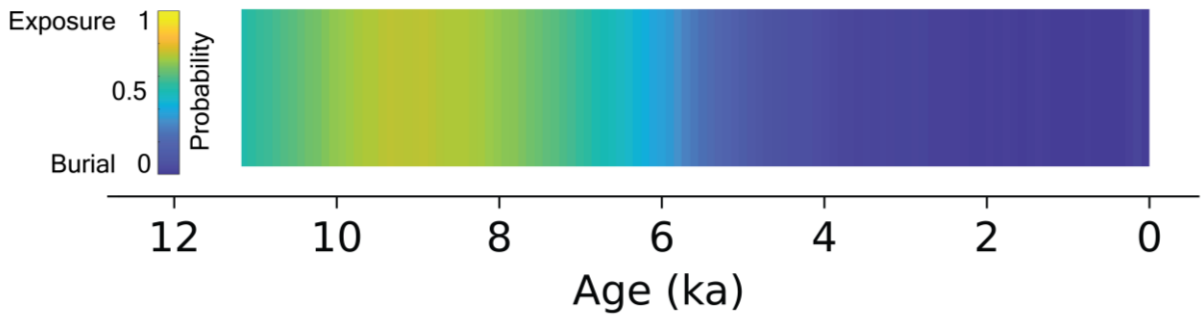

Fig. S9.
Results of a Monte Carlo forward model (*19*) which identifies exposure-burial histories consistent with the ^{14}C-^{10}Be concentrations measured in samples P12 and P13 at Charquini Norte Glacier (*26*). The plot shows a summary statistic of all the exposure-burial histories which successfully predicted both ^{14}C-^{10}Be concentrations within 3σ measurement uncertainty. A value of 1 indicates that all exposure-burial histories at a particular time slice predict exposure, while 0 represents the opposite. A value of 0.5 thereby represents half indicating exposure and half indicating burial. The calculated probability assumes that all successful histories are equally likely.

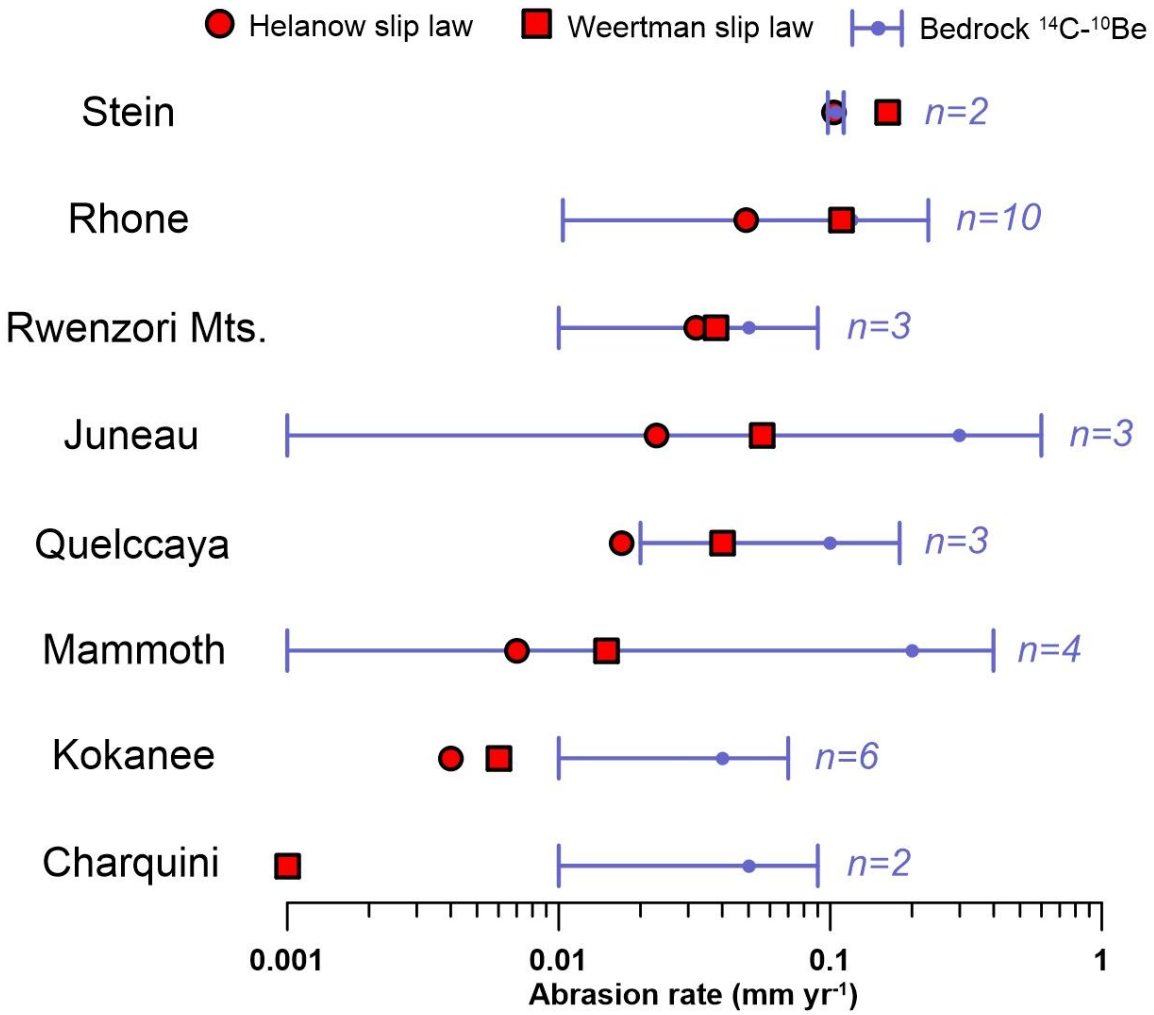

Fig. S10.
Validation of modeled abrasion rates for eight of the glaciers in Fig. 4. Red symbols show the model estimates using a power-based abrasion rule for two slip laws (*59*, *60*) (red symbols). Blue error bars show constraints from ^{14}C-^{10}Be measurements on proglacial bedrock (mean ± 1 standard deviation; n values give number of samples) (*17*, *19*, *26*, *37*, *47*). ^{14}C-^{10}Be samples interpreted as glacially plucked by the original authors were excluded.

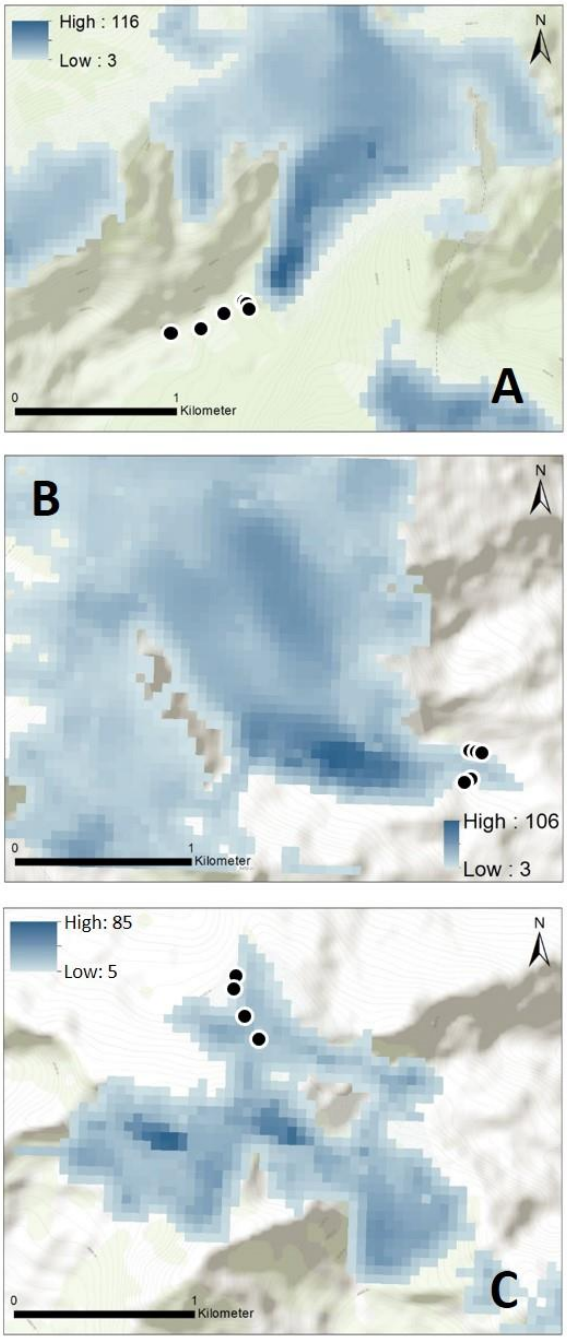

Fig. S11.

Ice thicknesses (m) for (**A**) Queshque Glacier, (**B**) Zongo Glacier, and (**C**) Charquini Norte Glacier based on 2017-2018 satellite image pairs **(*71*)**. Data are not available for Pan de Azucar Glacier. Black dots show bedrock sample locations.

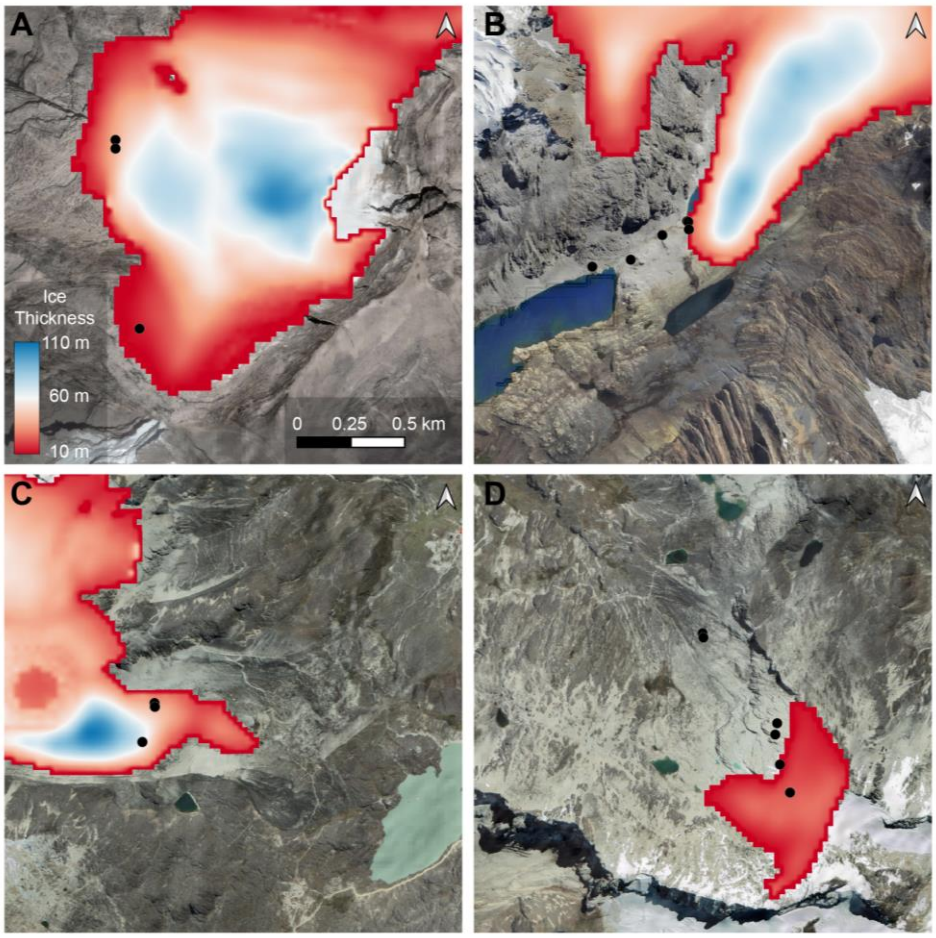

Fig. S12.

Ice thicknesses (m) ca. 2000 CE for (**A**) Pan de Azucar Glacier, (**B**) Queshque Glacier, (**C**) Zongo Glacier, and (**D**) Charquini Norte Glacier inferred from surface characteristics and ice flow dynamics (*57*). Ice thickness symbology and scale bar are the same in all panels. Black dots show bedrock sample locations.

Table S1. Sample information.

Sample	Latitude (DD)	Longitude (DD)	Elevation (m asl)	Thickness (cm)	Shielding
Pan de Azucar Glacier					
SNC-12-09	6.36569	-72.30404	4723	2.3	0.979
SNC-18-24	6.37353	-72.30497	4838	1.5	0.98
SNC-18-30	6.37316	-72.30504	4840	1.5	0.985
Queshque Glacier					
Que-1	-9.79249	-77.25158	4710	2.75	0.96
Que-2	-9.792516	-77.25153	4714	3	0.96
Que-3	-9.792832	-77.25150	4714	2	0.96
Que-4	-9.793069	-77.25262	4707	2	0.94
Que-5	-9.794099	-77.25394	4692	2.75	0.93
Que-6	-9.794391	-77.25555	4701	2.5	0.92
Charquini Norte Glacier					
P1	-16.29507	-68.10237	5130	2.9	0.97
P2	-16.29386	-68.10281	5131	3.3	0.97
P3	-16.29256	-68.10301	5099	4.8	0.97
P3bis	-16.29206	-68.10294	5099	3.1	0.97
P12	-16.28814	-68.10618	4911	3.7	0.97
P13	-16.28834	-68.10615	4915	4.3	0.97
Zongo Glacier					
Zon-1	-16.28062	-68.13677	4978	2.0	0.98
Zon-2	-16.28044	-68.13659	4975	3.5	0.98
Zon-3	-16.27877	-68.13613	4971	1.7	0.98
Zon-4	-16.27875	-68.13631	5005	2.0	0.99
Zon-5	-16.27875	-68.13642	5012	3	0.99

Table S2.
^{10}Be sample processing details. Uncertainties are 1σ.

Sample	Be Carrier Added (g)†	^{10}Be/^{9}Be* (10^{-15})	Quartz Mass (g)	^{10}Be^ (10^{3} atoms/g)	^{10}Be Blank
Pan de Azucar Glacier					
SNC-12-09	0.7775	3.51±0.64	20.0319	1.56±0.45	29-1, 29-2
SNC-18-24	0.7737	5.32±0.93	20.0862	2.72±0.63	29-1, 29-2
SNC-18-30	0.7727	3.46±0.67	20.0661	1.51±0.46	29-1, 29-2
Queshque Glacier					
Que-1	0.6735	4.25±0.10	34.8305	0.69±0.36	31-1, 31-9
Que-2	0.7017	4.12±0.92	36.7875	0.64±0.33	31-1, 31-9
Que-3	0.6965	3.38±0.94	40.4582	0.35±0.30	31-1, 31-9
Que-4	0.7034	4.22±1.06	21.128	1.17±0.64	31-1, 31-9
Que-5	0.6362	6.46±1.35	36.7035	1.20±0.42	31-1, 31-9
Que-6	0.6852	11.07±1.65	33.8202	3.03±0.60	31-1, 31-9
Charquini Norte Glacier					
P1	0.2810	1.30±0.23	5.5163	2.43±1.07	BLK_020819
P2	0.2906	1.66±0.27	6.8786	3.17±0.97	BLK_020819
P3	0.2828	1.63±0.29	5.4985	3.69±1.26	BLK_020819
P3bis	0.2872	1.91±0.30	5.6438	4.70±1.25	BLK_020819
P12	0.2872	30.10±1.09	6.2222	97.60±3.79	BLK_020819
P13	0.2857	31.40±1.93	5.2822	120.0±7.62	BLK_020819
Zongo Glacier					
Zon-1	0.7012	7.06±1.31	42.5175	1.36±0.39	31-1, 31-9
Zon-2	0.7195	10.40±1.49	34.9665	2.88±0.56	31-1, 31-9
Zon-3	0.7148	10.28±1.90	33.8695	2.90±0.71	31-1, 31-9
Zon-4	0.6809	7.31±1.27	30.2193	1.93±0.52	31-1, 31-9
Zon-5	0.7095	5.49±1.12	31.0091	1.30±0.47	31-1, 31-9

† Charquini Norte Glacier ^{10}Be carrier concentration: 1074 ppm. All other sites ^{10}Be carrier concentration: 251.6 ppm.
* ^{10}Be/^{9}Be ratios were measured by AMS at PRIME Lab and calibrated against the Revised ICN Standard (07KNSTD)
^ Blank-corrected concentration

Table S3.
^{14}C sample processing details. Uncertainties are 1σ.

Sample	Quartz Mass (g)	C Yield (µg)	Diluted C Mass (µg)	$^{14}C/C$*(10^{-14})	^{14}C^ (10^4 atoms/g)
Pan de Azucar Glacier					
SNC-12-09	5.0272	26.2	112.4	2.36±0.03	$1.59^{+0.57}_{-1.17}$
SNC-18-24	5.1179	32.3	99.3	2.25±0.03	$1.15^{+0.56}_{-1.15}$
SNC-18-30	4.4437	18.6	112.6	2.00±0.03	$1.35^{+0.65}_{-1.32}$
Queshque Glacier					
Que-1	5.004	4.2	92.6	2.48±0.03	$1.24^{+0.57}_{-1.18}$
Que-2	4.9398	3.5	111.3	1.79±0.02	$0.97^{+0.58}_{-0.97}$
Que-3	4.8881	4	102.6	2.24±0.03	$1.28^{+0.58}_{-1.20}$
Que-4	4.9383	3.8	112.2	2.10±0.03	$1.33^{+0.57}_{-1.20}$
Que-5	5.0353	3.5	100.4	2.60±0.03	$1.55^{+0.57}_{-1.17}$
Que-6	5.0219	4	112	2.60±0.03	$1.85^{+0.57}_{-1.17}$
Charquini Norte Glacier					
P1	2.036	3.5	111.7	1.11±0.02	$0.49^{+1.41}_{-0.49}$
P2	1.9909	2.9	115.8	97.89±0.02	$0.24^{+1.43}_{-0.24}$
P3	2.0402	3.4	109.8	1.40±0.02	$1.22^{+1.41}_{-1.22}$
P3bis	2.0998	3.7	92.6	1.68±0.03	$1.24^{+1.37}_{-1.24}$
P12	2.7070	2.6	95.3	5.25±0.06	$7.34^{+1.07}_{-2.18}$
P13	2.6746	2.6	113.3	5.87±0.05	$10.50^{+1.09}_{-2.20}$
Zongo Glacier					
Zon-1	4.8993	6.8	92	4.52±0.04	$3.17^{+0.59}_{-1.20}$
Zon-2	4.9913	9.4	113.3	2.86±0.04	$2.19^{+0.57}_{-1.18}$
Zon-3	5.021	10.4	113.1	1.76±0.04	$0.94^{+0.57}_{-0.94}$
Zon-4	4.9289	9.8	112.8	2.92±0.03	$2.28^{+0.58}_{-1.20}$
Zon-5	4.9992	5.7	113.4	20.99±0.12	$226.70^{+6.81}_{-12.10}$

* Carbon isotope ratios were measure by AMS at the National Ocean Sciences Accelerator Mass Spectrometer at Woods Hole Oceanographic Institution relative to the Oxalic Acid II primary standard (NIST SRM4990C)
^ Blank-corrected concentration

Table S4.
^{10}Be Blank Data. Uncertainties are 1σ.

Blank ID	Be carrier (g)	^{10}Be/^{9}Be (10^{-15})	^{10}Be (10^{4} atoms)
BLK_020819	0.2885	0.62±0.17	1.28±0.35
Blank_29-1	0.7648	0.99±0.40	1.27±0.52
Blank_29-2	0.7698	1.29±0.36	1.67±0.46
Blank_31-1	0.7737	1.68±0.53	2.19±0.69
Blank_31-9	0.6913	2.46±0.77	2.86±0.90

Table S5.
^{10}Be and ^{14}C concentrations expressed as years of equivalent surface exposure. 1σ external uncertainties.

Sample	Local ^{10}Be Prod Rate (atoms·g^{-1}·yr^{-1}) †	Local ^{14}C Prod Rate (atoms·g^{-1}·yr^{-1}) †	^{10}Be age* (yr)	^{14}C age* (yr)	Year Collected	Approx. Year Exposed	^{10}Be age corrected for recent exposure (yr)	^{14}C age corrected for recent exposure (yr)
Pan de Azucar Glacier								
SNC-12-09	38.1	114.5	41±12	138^{+50}_{-103}	2012	2012	37±10	138^{+50}_{-103}
SNC-18-24	40.2	120.2	68±16	95^{+47}_{-95}	2018	2018	61±14	95^{+47}_{-95}
SNC-18-30	40.4	120.9	37±11	111^{+54}_{-110}	2018	2018	34±10	111^{+54}_{-110}
Queshque Glacier								
Que-1	37.7	113.1	18±9	110^{+51}_{-104}	2019	2010	9±9	101^{+50}_{-101}
Que-2	37.7	113.3	17±9	85^{+51}_{-85}	2019	2010	8±9	76^{+51}_{-76}
Que-3	37.7	113.3	9±8	112^{+52}_{-107}	2019	2010	0±8	103^{+51}_{-103}
Que-4	36.8	110.5	32±17	120^{+53}_{-109}	2019	2005	18±17	106^{+52}_{-106}
Que-5	36.0	108.2	33±12	143^{+53}_{-109}	2019	1995	8±12	119^{+52}_{-109}
Que-6	35.9	107.9	87±17	171^{+53}_{-110}	2019	1990	58±17	112^{+53}_{-112}
Charquini Norte Glacier								
P1	47.9	140.9	51±22	34^{+101}_{-34}	2017	2015	49±22	32^{+101}_{-32}
P2	47.9	141.0	66±20	15^{+103}_{-15}	2017	2004	53±20	2^{+103}_{-2}
P3	47.2	139.2	78±26	87^{+101}_{-87}	2017	1985	46±26	55^{+101}_{-55}
P3bis	47.2	139.2	100±26	88^{+99}_{-88}	2017	1985	68±26	56^{+99}_{-56}
P12	43.4	128.95	2248±87	568^{+84}_{-170}	2017	1935	2166±87	486^{+84}_{-170}
P13	43.5	129.2	2755±175	812^{+85}_{-172}	2017	1935	2673±175	730^{+85}_{-172}
Zongo Glacier								
Zon-1	45.7	135.2	30±8	234^{+44}_{-89}	2019	2019	30±8	234^{+44}_{-89}
Zon-2	45.6	135.0	63±12	162^{+43}_{-88}	2019	2019	63±12	162^{+43}_{-88}
Zon-3	45.5	134.8	64±15	70^{+42}_{-70}	2019	2019	64±15	70^{+42}_{-70}
Zon-4	46.7	138.2	41±11	165^{+42}_{-87}	2019	2019	41±11	165^{+42}_{-87}
Zon-5	46.9	138.6	28±10	1635^{+50}_{-86}	2019	2019	28±10	1635^{+50}_{-86}

† Calculated using the University of Washington online cosmogenic calculator v3 with the LSDn scaling scheme and global production rate calibration dataset (*52*, *53*). Production rates account for sample thickness.
* Ages are calculated by dividing the measured concentration by the production rate.

Table S6.
Data used to estimate abrasion rates at glaciers in this study and prior work

Glacier	Mean Glacier Thickness[a] (m)	Ice-Surface Slope (°)	Estimated Erosion Rate[b] (mm yr^{-1})	Estimated Erosion Rate[c] (mm yr^{-1})	Lat. (DD)	Area (km^2)	Elev. (m)	RGI ID	GLIMS Analysis ID
Stein	68	21.10	0.103	0.163	47	8.0	2876	RGI60-11.01144	332642
Rhone	95	14.05	0.049	0.110	47	15.8	2950	RGI60-11.01238	332538
Zongo	44	23.99	0.046	0.051	-16	2.4	5380	RGI60-16.00543	770099
Queshque	40	24.31	0.035	0.037	-10	2.0	5080	RGI60-16.02060	767391
Rwenzori Mtns.*	42	23.50	0.032	0.038	0	0.4	4810	RGI60-16.01631	310587
Juneau Icefield	127	9.00	0.023	0.056	59	14.8	1560	RGI60-01.01310	1040666
Pan de Azucar	37	23.30	0.018	0.022	6	2.8	4840	RGI60-16.01363	311540
Quelccaya	85	12.24	0.017	0.040	-14	5.2	5460	RGI60-16.01251	769072
Mammoth	52	15.60	0.007	0.015	43	2.5	3660	RGI60-02.15964	766126
Kokanee	29	22.00	0.004	0.006	50	0.5	2560	RGI60-02.00145	390196
Conness	21	23.20	0.002	0.002	38	0.2	3600	RGI60-02.18788	764008
Charquini Norte	20	21.10	0.001	0.001	-16	0.2	5150	RGI60-16.00527	770108

[a] Farinotti et al. (*57*)
[b] Using Helanow et al. slip law (*60*)
[c] Using Weertman slip law (*59*)
* No RGI outline exists, used the nearest glacier in RGI (Stanley Glacier)
All area, slope, and elevation data from Randolph Glacier Inventory (RGI) (*58*) and Global Land Ice Measurements from Space Initiative (GLIMS) database (*73*).
Elevation is mean or median depending on availability in RGI/GLIMS.
Ice surface slope and mean glacier thickness are based on glacier positions around the turn of the century or 2000 CE.

References and Notes

1. R. Hugonnet, R. McNabb, E. Berthier, B. Menounos, C. Nuth, L. Girod, D. Farinotti, M. Huss, I. Dussaillant, F. Brun, A. Kääb, Accelerated global glacier mass loss in the early twenty-first century. *Nature* **592**, 726–731 (2021). doi:10.1038/s41586-021-03436-z Medline

2. B. Marzeion, J. G. Cogley, K. Richter, D. Parkes, Glaciers. Attribution of global glacier mass loss to anthropogenic and natural causes. *Science* **345**, 919–921 (2014). doi:10.1126/science.1254702 Medline

3. J. Hansen, P. Kharecha, M. Sato, V. Masson-Delmotte, F. Ackerman, D. J. Beerling, P. J. Hearty, O. Hoegh-Guldberg, S.-L. Hsu, C. Parmesan, J. Rockstrom, E. J. Rohling, J. Sachs, P. Smith, K. Steffen, L. Van Susteren, K. von Schuckmann, J. C. Zachos, Assessing "dangerous climate change": Required reduction of carbon emissions to protect young people, future generations and nature. *PLOS ONE* **8**, e81648 (2013). doi:10.1371/journal.pone.0081648 Medline

4. V. Masson-Delmotte, P. Zhai, H. O. Portner, D. Roberts, J. Skea, P. R. Shukla, A. Pirani, W. Moufouma-Okia, C. Pean, R. Pidcock, S. Connors, J. B. R. Matthews, Y. Chen, M. I. Gomis, E. Lonnoy, T. Maycock, M. Tignor, T. Waterfield, "Global warming of 1.5°C: An IPCC Special Report on the impacts of global warming of 1.5°C above pre-industrial levels and related global greenhouse gas emission pathways, in the context of strengthening the global response to the threat of climate change, sustainable development, and efforts to eradicate poverty" (2018); https://www.ipcc.ch/sr15/.

5. R. Monastersky, Anthropocene: The human age. *Nature* **519**, 144–147 (2015). doi:10.1038/519144a Medline

6. V. Masson-Delmotte, P. Zhai, A. Pirani, S. L. Connors, C. Pean, S. Berger, N. Caud, Y. Chen, L. Goldfarb, M. I. Gomis, M. I. Huang, K. Leitzell, E. Lonnoy, J. B. R. Matthews, T. K. Maycook, T. Waterfield, O. Yelekci, R. Yu, R. Zhou, "Climate Change 2021: The Physical Science Basis. Working Group I Contribution to the Sixth Assessment Report of the Intergovernmental Panel on Climate Change" (2021); https://www.ipcc.ch/report/ar6/wg1/.

7. O. N. Solomina, R. S. Bradley, D. A. Hodgson, S. Ivy-Ochs, V. Jomelli, A. N. Mackintosh, A. Nesje, L. A. Owen, H. Wanner, G. C. Wiles, N. E. Young, Holocene glacier fluctuations. *Quat. Sci. Rev.* **111**, 9–34 (2015). doi:10.1016/j.quascirev.2014.11.018

8. B. Marzeion, G. Kaser, F. Maussion, N. Champollion, Limited influence of climate change mitigation on short-term glacier mass loss. *Nat. Clim. Chang.* **8**, 305–308 (2018). doi:10.1038/s41558-018-0093-1

9. D. Kaufman, N. McKay, C. Routson, M. Erb, C. Dätwyler, P. S. Sommer, O. Heiri, B. Davis, Holocene global mean surface temperature, a multi-method reconstruction approach. *Sci. Data* **7**, 201 (2020). doi:10.1038/s41597-020-0530-7 Medline

10. P. Huybers, W. Curry, Links between annual, Milankovitch and continuum temperature variability. *Nature* **441**, 329–332 (2006). doi:10.1038/nature04745 Medline

11. R. S. Bradley, M. Vuille, H. F. Diaz, W. Vergara, Climate change. Threats to water supplies in the tropical Andes. *Science* **312**, 1755–1756 (2006). doi:10.1126/science.1128087 Medline

12. J. Aguilar-Lome, R. Espinoza-Villar, J.-C. Espinoza, J. Rojas-Acuña, B. L. Willems, W.-M. Leyva-Molina, Elevation-dependent warming of land surface temperatures in the Andes assessed using MODIS LST time series (2000–2017). *Int. J. Appl. Earth Obs. Geoinf.* **77**, 119–128 (2019). doi:10.1016/j.jag.2018.12.013

13. G. Kaser, H. Osmaston, *Tropical Glaciers* (Cambridge Univ. Press, digitally printed first paperback version, with corrections, 2006).

14. K. Lamantia, L. Thompson, M. Davis, E. Mosley-Thompson, H. Stahl, Unique Collections of 14 C-Dated Vegetation Reveal Mid-Holocene Fluctuations of the Quelccaya Ice Cap, Peru. *J. Geophys. Res. Earth Surf.* **128**, e2023JF007297 (2023). doi:10.1029/2023JF007297

15. N. D. Stansell, M. B. Abbott, M. B. Diaz, J. M. Licciardi, B. G. Mark, P. J. Polissar, D. T. Rodbell, T. Y. Shutkin, Pre-industrial Holocene glacier variability in the tropical Andes as context for anthropogenically driven ice retreat. *Global Planet. Change* **229**, 104242 (2023). doi:10.1016/j.gloplacha.2023.104242

16. D. T. Rodbell, G. O. Seltzer, B. G. Mark, J. A. Smith, M. B. Abbott, Clastic sediment flux to tropical Andean lakes: Records of glaciation and soil erosion. *Quat. Sci. Rev.* **27**, 1612–1626 (2008). doi:10.1016/j.quascirev.2008.06.004

17. B. M. Goehring, J. M. Schaefer, C. Schluechter, N. A. Lifton, R. C. Finkel, A. J. T. Jull, N. Akcar, R. B. Alley, The Rhone Glacier was smaller than today for most of the Holocene. *Geology* **39**, 679–682 (2011). doi:10.1130/G32145.1

18. Materials and methods are available as supplementary materials.

19. A. C. Vickers, J. D. Shakun, B. M. Goehring, A. Gorin, M. A. Kelly, M. S. Jackson, A. Doughty, J. Russell, Similar Holocene glaciation histories in tropical South America and Africa. *Geology* **49**, 140–144 (2021). doi:10.1130/G48059.1

20. E. A. Sagredo, S. Rupper, T. V. Lowell, Sensitivities of the equilibrium line altitude to temperature and precipitation changes along the Andes. *Quat. Res.* **81**, 355–366 (2014). doi:10.1016/j.yqres.2014.01.008

21. B. G. Mark, G. O. Seltzer, Evaluation of recent glacier recession in the Cordillera Blanca, Peru (AD 1962–1999): Spatial distribution of mass loss and climatic forcing. *Quat. Sci. Rev.* **24**, 2265–2280 (2005). doi:10.1016/j.quascirev.2005.01.003

22. M. Vuille, B. Francou, P. Wagnon, I. Juen, G. Kaser, B. G. Mark, R. S. Bradley, Climate change and tropical Andean glaciers: Past, present and future. *Earth Sci. Rev.* **89**, 79–96 (2008). doi:10.1016/j.earscirev.2008.04.002

23. J. L. Ceballos, C. Euscátegui, J. Ramírez, M. Cañon, C. Huggel, W. Haeberli, H. Machguth, Fast shrinkage of tropical glaciers in Colombia. *Ann. Glaciol.* **43**, 194–201 (2006). doi:10.3189/172756406781812429

24. V. Jomelli, M. Khodri, V. Favier, D. Brunstein, M.-P. Ledru, P. Wagnon, P.-H. Blard, J.-E. Sicart, R. Braucher, D. Grancher, D. L. Bourlès, P. Braconnot, M. Vuille, Irregular tropical glacier retreat over the Holocene epoch driven by progressive warming. *Nature* **474**, 196–199 (2011). doi:10.1038/nature10150 Medline

25. V. Jomelli, V. Favier, M. Vuille, R. Braucher, L. Martin, P.-H. Blard, C. Colose, D. Brunstein, F. He, M. Khodri, D. L. Bourlès, L. Leanni, V. Rinterknecht, D. Grancher, B. Francou, J. L. Ceballos, H. Fonseca, Z. Liu, B. L. Otto-Bliesner, A major advance of tropical Andean glaciers during the Antarctic cold reversal. *Nature* **513**, 224–228 (2014). doi:10.1038/nature13546 Medline

26. V. Jomelli, D. Swingedouw, M. Vuille, V. Favier, B. Goehring, J. Shakun, R. Braucher, I. Schimmelpfennig, L. Menviel, A. Rabatel, L. C. P. Martin, P.-H. Blard, T. Condom, M. Lupker, M. Christl, Z. He, D. Verfaillie, A. Gorin, G. Aumaître, D. L. Bourlès, K. Keddadouche, In-phase millennial-scale glacier changes in the tropics and North Atlantic regions during the Holocene. *Nat. Commun.* **13**, 1419 (2022). doi:10.1038/s41467-022-28939-9 Medline

27. N. D. Stansell, J. M. Licciardi, D. T. Rodbell, B. G. Mark, Tropical ocean-atmospheric forcing of Late Glacial and Holocene glacier fluctuations in the Cordillera Blanca, Peru. *Geophys. Res. Lett.* **44**, 4176–4185 (2017). doi:10.1002/2016GL072408

28. N. E. Young, J. P. Briner, J. Maurer, J. M. Schaefer, ^{10}Be measurements in bedrock constrain erosion beneath the Greenland Ice Sheet margin. *Geophys. Res. Lett.* **43**, 11,708–11,719 (2016). doi:10.1002/2016GL070258

29. J. D. Shakun, L. B. Corbett, P. R. Bierman, K. Underwood, D. M. Rizzo, S. R. Zimmerman, M. W. Caffee, T. Naish, N. R. Golledge, C. C. Hay, Minimal East Antarctic Ice Sheet retreat onto land during the past eight million years. *Nature* **558**, 284–287 (2018). doi:10.1038/s41586-018-0155-6 Medline

30. L. G. Thompson, E. Mosley-Thompson, M. E. Davis, V. S. Zagorodnov, I. M. Howat, V. N. Mikhalenko, P.-N. Lin, Annually resolved ice core records of tropical climate variability over the past ~1800 years. *Science* **340**, 945–950 (2013). doi:10.1126/science.1234210 Medline

31. R. Neukom, N. Steiger, J. J. Gómez-Navarro, J. Wang, J. P. Werner, No evidence for globally coherent warm and cold periods over the preindustrial Common Era. *Nature* **571**, 550–554 (2019). doi:10.1038/s41586-019-1401-2 Medline

32. B. L. Konecky, N. P. McKay, G. M. Falster, S. L. Stevenson, M. J. Fischer, A. R. Atwood, D. M. Thompson, M. D. Jones, J. J. Tyler, K. L. DeLong, B. Martrat, E. K. Thomas, J. L. Conroy, S. G. Dee, L. Jonkers, O. V. Churakova, Z. Kern, T. Opel, T. J. Porter, H. R. Sayani, G. Skrzypek, Iso2k Project Members, Globally coherent water cycle response to temperature change during the past two millennia. *Nat. Geosci.* **16**, 997–1004 (2023). doi:10.1038/s41561-023-01291-3

33. D. S. Kaufman, E. Broadman, Revisiting the Holocene global temperature conundrum. *Nature* **614**, 425–435 (2023). doi:10.1038/s41586-022-05536-w Medline

34. S. J. Cook, D. A. Swift, M. P. Kirkbride, P. G. Knight, R. I. Waller, The empirical basis for modelling glacial erosion rates. *Nat. Commun.* **11**, 759 (2020). doi:10.1038/s41467-020-14583-8 Medline

35. D. D. Hansen, J. P. Brooks, L. K. Zoet, N. T. Stevens, L. Smith, C. E. Bate, B. J. Jahnke, A power-based abrasion law for use in landscape evolution models. *Geology* **51**, 273–277 (2023). doi:10.1130/G50673.1

36. M. Réveillet, A. Rabatel, F. Gillet-Chaulet, A. Soruco, Simulations of changes to Glaciar Zongo, Bolivia (16° S), over the 21st century using a 3-D full-Stokes model and CMIP5 climate projections. *Ann. Glaciol.* **56**, 89–97 (2015). doi:10.3189/2015AoG70A113

37. A. G. Jones, S. A. Marcott, A. L. Gorin, T. M. Kennedy, J. D. Shakun, B. M. Goehring, B. Menounos, D. H. Clark, M. Romero, M. W. Caffee, Four North American glaciers advanced past their modern positions thousands of years apart in the Holocene. *Cryosphere* **17**, 5459–5475 (2023). doi:10.5194/tc-17-5459-2023

38. M. Koppes, B. Hallet, E. Rignot, J. Mouginot, J. S. Wellner, K. Boldt, Observed latitudinal variations in erosion as a function of glacier dynamics. *Nature* **526**, 100–103 (2015). doi:10.1038/nature15385 Medline

39. F. Herman, O. Beyssac, M. Brughelli, S. N. Lane, S. Leprince, T. Adatte, J. Y. Y. Lin, J.-P. Avouac, S. C. Cox, Erosion by an Alpine glacier. *Science* **350**, 193–195 (2015). doi:10.1126/science.aab2386 Medline

40. G. Poveda, K. Pineda, Reassessment of Colombia's tropical glaciers retreat rates: Are they bound to disappear during the 2010–2020 decade? *Adv. Geosci.* **22**, 107–116 (2009). doi:10.5194/adgeo-22-107-2009

41. S. Hastenrath, *Climate Dynamics of the Tropics* (Springer, 1991).

42. P. J. Polissar, M. B. Abbott, A. P. Wolfe, M. Vuille, M. Bezada, Synchronous interhemispheric Holocene climate trends in the tropical Andes. *Proc. Natl. Acad. Sci. U.S.A.* **110**, 14551–14556 (2013). doi:10.1073/pnas.1219681110 Medline

43. B. W. Bird, O. Rudloff, J. Escobar, W. P. Gilhooly III, A. Correa-Metrio, M. Vélez, P. J. Polissar, Paleoclimate support for a persistent dry island effect in the Colombian Andes during the last 4700 years. *Holocene* **28**, 217–228 (2018). doi:10.1177/0959683617721324

44. B. A. Steinman, N. D. Stansell, M. E. Mann, C. A. Cooke, M. B. Abbott, M. Vuille, B. W. Bird, M. S. Lachniet, A. Fernandez, Interhemispheric antiphasing of neotropical precipitation during the past millennium. *Proc. Natl. Acad. Sci. U.S.A.* **119**, e2120015119 (2022). doi:10.1073/pnas.2120015119 Medline

45. S. L. Pendleton, G. H. Miller, N. Lifton, S. J. Lehman, J. Southon, S. E. Crump, R. S. Anderson, Rapidly receding Arctic Canada glaciers revealing landscapes

continuously ice-covered for more than 40,000 years. *Nat. Commun.* **10**, 445 (2019). doi:10.1038/s41467-019-08307-w Medline

46. Berkeley Earth (2024); www.berkeleyearth.org.

47. I. Schimmelpfennig, J. M. Schaefer, J. Lamp, V. Godard, R. Schwartz, E. Bard, T. Tuna, N. Akçar, C. Schlüchter, S. Zimmerman, ASTER Team, Glacier response to Holocene warmth inferred from in situ ^{10}Be and ^{14}C bedrock analyses in Steingletscher's forefield (central Swiss Alps). *Clim. Past* **18**, 23–44 (2022). doi:10.5194/cp-18-23-2022

48. L. B. Corbett, P. R. Bierman, D. H. Rood, An approach for optimizing in situ cosmogenic 10Be sample preparation. *Quat. Geochronol.* **33**, 24–34 (2016). doi:10.1016/j.quageo.2016.02.001

49. E. G. Ceperley, S. A. Marcott, J. E. Rawling III, L. K. Zoet, S. R. H. Zimmerman, The role of permafrost on the morphology of an MIS 3 moraine from the southern Laurentide Ice Sheet. *Geology* **47**, 440–444 (2019). doi:10.1130/G45874.1

50. B. M. Goehring, J. Wilson, K. Nichols, A fully automated system for the extraction of in situ cosmogenic carbon-14 in the Tulane University cosmogenic nuclide laboratory. *Nucl. Instrum. Methods Phys. Res. B* **455**, 284–292 (2019). doi:10.1016/j.nimb.2019.02.006

51. G. Balco, N. Brown, K. Nichols, R. A. Venturelli, J. Adams, S. Braddock, S. Campbell, B. Goehring, J. S. Johnson, D. H. Rood, K. Wilcken, B. Hall, J. Woodward, Reversible ice sheet thinning in the Amundsen Sea Embayment during the Late Holocene. *Cryosphere* **17**, 1787–1801 (2023). doi:10.5194/tc-17-1787-2023

52. N. Lifton, T. Sato, T. J. Dunai, Scaling in situ cosmogenic nuclide production rates using analytical approximations to atmospheric cosmic-ray fluxes. *Earth Planet. Sci. Lett.* **386**, 149–160 (2014). doi:10.1016/j.epsl.2013.10.052

53. G. Balco, J. O. Stone, N. A. Lifton, T. J. Dunai, A complete and easily accessible means of calculating surface exposure ages or erosion rates from 10Be and 26Al measurements. *Quat. Geochronol.* **3**, 174–195 (2008). doi:10.1016/j.quageo.2007.12.001

54. A. Rabatel, A. Machaca, B. Francou, V. Jomelli, Glacier recession on Cerro Charquini (16° S), Bolivia, since the maximum of the Little Ice Age (17th century). *J. Glaciol.* **52**, 110–118 (2006). doi:10.3189/172756506781828917

55. A. Soruco, C. Vincent, B. Francou, J. F. Gonzalez, Glacier decline between 1963 and 2006 in the Cordillera Real, Bolivia. *Geophys. Res. Lett.* **36**, L03502 (2009). doi:10.1029/2008GL036238

56. K. Cuffey, W. S. B. Paterson, *The Physics of Glaciers* (Butterworth-Heinemann/Elsevier, ed. 4, 2010).

57. D. Farinotti, M. Huss, J. J. Fürst, J. Landmann, H. Machguth, F. Maussion, A. Pandit, A consensus estimate for the ice thickness distribution of all glaciers on Earth. *Nat. Geosci.* **12**, 168–173 (2019). doi:10.1038/s41561-019-0300-3

58. RGI Consortium, Randolph Glacier Inventory - A Dataset of Global Glacier Outlines, Version 7, National Snow and Ice Data Center (2024); https://doi.org/10.5067/F6JMOVY5NAVZ.

59. J. Weertman, On the Sliding of Glaciers. *J. Glaciol.* **3**, 33–38 (1957). doi:10.3189/S0022143000024709

60. C. Helanow, N. R. Iverson, J. B. Woodard, L. K. Zoet, A slip law for hard-bedded glaciers derived from observed bed topography. *Sci. Adv.* **7**, eabe7798 (2021). doi:10.1126/sciadv.abe7798 Medline

61. L. K. Zoet, N. R. Iverson, Rate-weakening drag during glacier sliding. *J. Geophys. Res. Earth Surf.* **121**, 1206–1217 (2016). doi:10.1002/2016JF003909

62. J. B. Woodard, L. K. Zoet, N. R. Iverson, C. Helanow, Variations in Hard-Bedded Topography Beneath Glaciers. *J. Geophys. Res. Earth Surf.* **126**, e2021JF006326 (2021). doi:10.1029/2021JF006326

63. M. N. Koppes, D. R. Montgomery, The relative efficacy of fluvial and glacial erosion over modern to orogenic timescales. *Nat. Geosci.* **2**, 644–647 (2009). doi:10.1038/ngeo616

64. H. Wittmann, F. Von Blanckenburg, T. Kruesmann, K. P. Norton, P. W. Kubik, Relation between rock uplift and denudation from cosmogenic nuclides in river sediment in the Central Alps of Switzerland. *J. Geophys. Res. Earth Surf.* **112**, F04010 (2007). doi:10.1029/2006JF000729

65. V. Ganti, C. von Hagke, D. Scherler, M. P. Lamb, W. W. Fischer, J.-P. Avouac, Time scale bias in erosion rates of glaciated landscapes. *Sci. Adv.* **2**, e1600204 (2016). doi:10.1126/sciadv.1600204 Medline

66. V. Rull, M. B. Abbott, P. J. Polissar, A. P. Wolfe, M. Bezada, R. S. Bradley, 15,000-yr Pollen Record of Vegetation change in the High Altitude Tropical Andes at Laguna Verde Alta, Venezuela. *Quat. Res.* **64**, 308–317 (2005). doi:10.1016/j.yqres.2005.08.014

67. N. D. Stansell, P. J. Polissar, M. B. Abbott, M. Bezada, B. A. Steinman, C. Braun, Proglacial lake sediment records reveal Holocene climate changes in the Venezuelan Andes. *Quat. Sci. Rev.* **89**, 44–55 (2014). doi:10.1016/j.quascirev.2014.01.021

68. K. Huh, M. Baraër, B. Mark, Y. Ahn, Evaluating Glacier Volume Changes since the Little Ice Age Maximum and Consequences for Stream Flow by Integrating Models of Glacier Flow and Hydrology in the Cordillera Blanca, Peruvian Andes. *Water* **10**, 1732 (2018). doi:10.3390/w10121732

69. N. D. Stansell, D. T. Rodbell, M. B. Abbott, B. G. Mark, Proglacial lake sediment records of Holocene climate change in the western Cordillera of Peru. *Quat. Sci. Rev.* **70**, 1–14 (2013). doi:10.1016/j.quascirev.2013.03.003

70. M. Vuille, R. S. Bradley, M. Werner, F. Keimig, 20th Century Climate Change in the Tropical Andes: Observations and Model Results. *Clim. Change* **59**, 75–99 (2003). doi:10.1023/A:1024406427519

71. R. Millan, J. Mouginot, A. Rabatel, M. Morlighem, Ice velocity and thickness of the world's glaciers. *Nat. Geosci.* **15**, 124–129 (2022). doi:10.1038/s41561-021-00885-z

72. N. D. Stansell, B. G. Mark, D. T. Licciardi, D. T. Rodbell, J. G. Fairman, F. S. Schoessow, T. Y. Shutkin, M. Sorensen, Energy mass balance and flow modeling of early Holocene glaciers in the Queshque valley, Cordillera Blanca, Peru. *Quat. Sci. Rev.* **281**, 107414 (2022). doi:10.1016/j.quascirev.2022.107414

73. GLIMS Consortium, GLIMS Glacier Database, Version 1, National Snow and Ice Data Center (2024); https://doi.org/10.7265/N5V98602.